

# Structure and Evolution of Clay-Organic Nanocomposites in Three Leading Shales in China

Yuantao Gu<sup>1</sup>, Quan Wan<sup>2</sup>, Xiaoxia Li<sup>1</sup>, Tao Han<sup>2</sup>, Shuguang Yang<sup>2,3</sup>, Qinhong Hu<sup>\*4,5</sup>



1. School of Resources and Environment, Henan University of Engineering, Zhengzhou 451191, China

2. State Key Laboratory of Ore Deposit Geochemistry, Institute of Geochemistry, Chinese Academy of Sciences, Guiyang 550081, China

3. University of Chinese Academy of Sciences, Beijing 100049, China

4. Shandong Provincial Key Laboratory of Deep Oil and Gas, China University of Petroleum (East China), Qingdao 266580, China

5. University of Texas at Arlington, Arlington Texas 76019, USA

 Yuantao Gu: <https://orcid.org/0000-0003-2655-2981>;  Qinhong Hu: <https://orcid.org/0000-0002-4782-319X>

**ABSTRACT:** Organic matter (OM) in shales occurs as nanometer-sized intercalations with clay minerals that are termed as clay-organic nanocomposites; however, the OM occurrence in nanocomposites at different stages of maturation is still unclear, and the co-evolution process of OM and clay under burial is not well understood. To reveal the variation of OM occurrence and clarify the relationship between petroleum generation of OM & transformation of clay minerals in nanocomposites as a function of maturity, this study investigates the structure and clay-OM association in 44 samples from three leading shales at different maturity stages from two basins in China. A total of 15 samples of lacustrine shale from upper Triassic Yanchang Formation, 15 samples of marine shale from Lower Silurian Longmaxi Formation, and 14 samples of marine shale from Lower Cambrian Niutitang Formation were analyzed based on organic geochemistry, X-ray diffraction (XRD), and field emission-scan electron microscopy (FE-SEM), focused ion beam (FIB) sample preparation and consequent high resolution-transmission electron microscopy (HR-TEM) observations combined with energy dispersive spectroscopy (EDS). The results from this study show that most shale samples are organic-rich, and these three shales represent thermal evolutionary process from oil-window mature to overmature in a sequence of Triassic Yanchang, Silurian Longmaxi, and Cambrian Niutitang formations. Thorough observations indicate that sub-parallel bands of clays and intermingling of detrital minerals (such as quartz) dominate the nanocomposites in the Yanchang samples. While for Longmaxi and Niutitang shales, abundant nanopores and pyrite nanoparticles are observed in nanocomposites with features of layered distributions of OM and clay minerals. The structural investigation of nanocomposites shows that organic carbon between multi-layers dominates the OM occurrence in nanocomposites, which significantly extends the traditional opinion of OM-clay association. At an oil-window mature stage, the fluctuational interlayer spacing and a certain intensity of the carbon peak observed in the EDS spectra for corresponding clays provide a visual evidence of the organic molecules accessing the monolayer spaces of smectite. With the evolutionary process of nanocomposites in shale and petroleum generation of OM & mineral transformation (illitization of smectite) running in parallel, it is inferred that the organic molecules migrate from monolayer spaces as gaseous hydrocarbons are generated, and eventually form stable clay-organic nanocomposites at an overmature stage. The results presented here will contribute to an improved understanding of diagenesis and organic-inorganic interactions in OM-rich shales.

**KEY WORDS:** organic matter, shale, clay-organic nanocomposites, structure, hydrocarbons.

## 0 INTRODUCTION

The complexation of clay minerals and organic matter (OM) at nanoscales, termed as clay-organic nanocomposites in the literature, has been proposed as a significant mechanism to

\*Corresponding author: [huqinhong@upc.edu.cn](mailto:huqinhong@upc.edu.cn)

© China University of Geosciences (Wuhan) and Springer-Verlag GmbH Germany, Part of Springer Nature 2023

Manuscript received December 8, 2021.

Manuscript accepted July 23, 2022.

preserve OM in sediments (Zhu H J et al., 2020; Rahman et al., 2018; Zhu X J et al., 2018; Kennedy et al., 2014; Cai et al., 2013; Lu et al., 2013). Several studies have been carried out on the relationship between, and the complexation of, OM and clay minerals during the sedimentation and diagenesis of shales (Cai et al., 2020, 2007; Zhu H J et al., 2020; Zhu X J et al., 2018; Bu et al., 2017; Yang et al., 2015; Kennedy et al., 2014). The complexation of OM and clay minerals can occur by means of hydrogen bonding, ionic and electrostatic interactions, and van der Waals force (Yariv and Cross, 2002). The positive correlation between total organic carbon (TOC) and

detrital contents in argillaceous sediments was first demonstrated by Aplin et al. (1992). Kennedy et al. (2002) also confirmed the positive relation between clay minerals and OM in black shale. From high resolution-transmission electron microscopy (HR-TEM) images of nanocomposites, Kennedy et al. (2014) showed that organic carbon is not present as discrete pelagic grains, but is dispersed and dominantly associated with mineral surfaces, resulting in a strong positive relation between mineral surface area and TOC contents. Furthermore, with an increasing thermal maturity (as reflected in vitrinite reflectance % $R_o$ ), the mineral surface area tends to decrease, which is probably due to the illitization of smectite during maturation, leading to the collapse of interlayer space (Yuan, 2018; Lanson et al., 2009; Meunier and Velde, 1989). This mineral transformation process is often accompanied by the recombination of OM and clay minerals, changing the structural characteristics of nanocomposites (Berthonneau et al., 2016; Kennedy et al., 2014). Hence, both sedimentation and then later thermal evolution, as well as petroleum generation, will control the complexation nature of OM and clay minerals in OM-rich shales.

The complexation between OM and clay minerals has been explored through laboratory experiments (Bu et al., 2017; Yang et al., 2015; Xu, 2013). For example, Bu et al. (2017) conducted a simulation reaction of montmorillonite and OM, and found that the complexation of OM and clay minerals greatly affected the pyrolytic reaction of OM. In the pyrolysis process, the solid acidity of montmorillonite made a difference to the composition and yield of the pyrolysis products, and a catalysis or pyrolysis-inhibiting effect during the pyrolysis of a given OM mainly depended on the nature of the model organic compound and clay-OM complexation (Bu et al., 2017). In addition, natural samples have also been used to analyze the structure of nanocomposites (e.g., Zhu et al., 2020; Berthonneau et al., 2016; Kennedy et al., 2014), and it was shown that in low maturity shales, OM and smectite layers formed both surface and interlayer complexes. With an increasing thermal maturity, the OM and clay layers that form the interlayer complexes tend to separate due to the illitization of smectite (Berthonneau et al., 2016), which probably leads to a change in the relationship between OM and clay layers. However, while most studies are mainly directed at the correlation between OM and clay minerals (e.g., Berthonneau et al., 2016; Kennedy et al., 2014), the variation of OM occurrence in nanocomposites at different stages of maturation is still unclear, and the co-evolution process of OM and clay minerals under burial is not well understood.

Therefore, the aim of this work is to reveal the variation of OM occurrence, and clarify the relationship between petroleum generation of OM and transformation of clay minerals in nanocomposites as a function of increasing thermal maturity. A total of 44 shale samples were selected from three formations namely, the Triassic Yanchang, Silurian Longmaxi, and Cambrian Niutitang formations, to investigate the structural characteristics of clay-organic nanocomposites by utilizing X-ray diffraction (XRD), field emission-scanning electron microscopy (FE-SEM), and focused ion beam (FIB) sample preparation and HR-TEM. Based on the results, we are able to confirm the OM occurrence in nanocomposites at different evolution stages, specify the co-evolution process of OM and clay minerals with re-

spect to thermal maturity, and propose a scheme to describe the evolution of nanocomposites in organic-rich shales to augment the understanding of diagenesis and petroleum generation of source rocks, as well as organic-inorganic interactions.

## 1 GEOLOGICAL SETTING

The Ordos Basin is located in northern-central China (Duan et al., 2008; Dai et al., 2005), as the second-largest (by area) sedimentary basin in China. It consists of six tectonic units: the Yimeng uplift, the Weibei uplift, the Tianhuan depression, the western edge thrust belt, the Jinxi fold belt, and the central Yishan slope (Fig. 1c) (Guo et al., 2014; Duan et al., 2008). The Late Triassic lacustrine shale from Yanchang is the most important source rock in Ordos Basin, and it is sub-divided into 10 members (numbered as Chang 1 to Chang 10 from top to bottom). Of these, the Chang 7 member has the material basis for shale oil occurrence and accumulation. In addition, the shale oil reserved in Chang 7 member has a great accumulation and favorable properties for flowing in nano-scale pores and throats (Yang et al., 2016). Fifteen Yanchang samples used in this work were sampled from an oil production well in the Chang 7 member, located in the eastern edge of the Yishan slope (Location Y on Fig. 1c).

The Sichuan Basin is the largest petroliferous basin in South China and also the most successful area in China for the exploitation of shale gas (Dong et al., 2016). In and around the basin, marine shales, such as Longmaxi and Niutitang, have a large potential for shale gas production. Longmaxi and Niutitang shales in the research area have different burial history: the maximum burial depth is approximately 6 500 m for Longmaxi shale, considerably less than in the Niutitang shale (9 000 m) that consequently being subjected to higher temperatures and pressures (Liu et al., 2016). In addition, Longmaxi shale became overmature with respect to petroleum generation in the Late Cretaceous (approximately 80 Ma), while Niutitang shale reached over-maturity in the Late Permian (approximately 250 Ma) (Cao et al., 2015; Jiang et al., 2015). Thus, Niutitang shale has experienced more substantial thermal evolution than Longmaxi shale. Fifteen Longmaxi samples were taken from an outcrop section in the eastern of Dian-Qian north depression (Location L on Fig. 1b), and another 14 Niutitang samples were collected from a well located in the east of the central Guizhou uplift (Location N in Fig. 1b).

The sedimentary environment determines the abundance, type and maceral of OM in shale (Song et al., 2019). Due to differences in sedimentary environment, different types of OM occur in our samples from three formations, and further affect petroleum generation potential of shale. The kerogen in Chang 7 member from Ordos Basin occurs as type II and a small fraction of type III under the deep to semi-deep lacustrine deposition. Among the macerals, sapropelinite is the most prevalent, and vitrinite and inertinite take second place (Wang et al., 2014). Both Longmaxi and Niutitang shales in and around Sichuan Basin were deposited in neritic shelf environment, and the sources of OM were dominated by various planktic algae (Liu et al., 2022; Wang et al., 2021; Song et al., 2019). The major kerogen type for both shales is type I, and the macerals occur mainly as bitumen, accompanied by a small percentage of sapropelinite (Song et al., 2019; Jiang, 2018; Zhao et al., 2016).

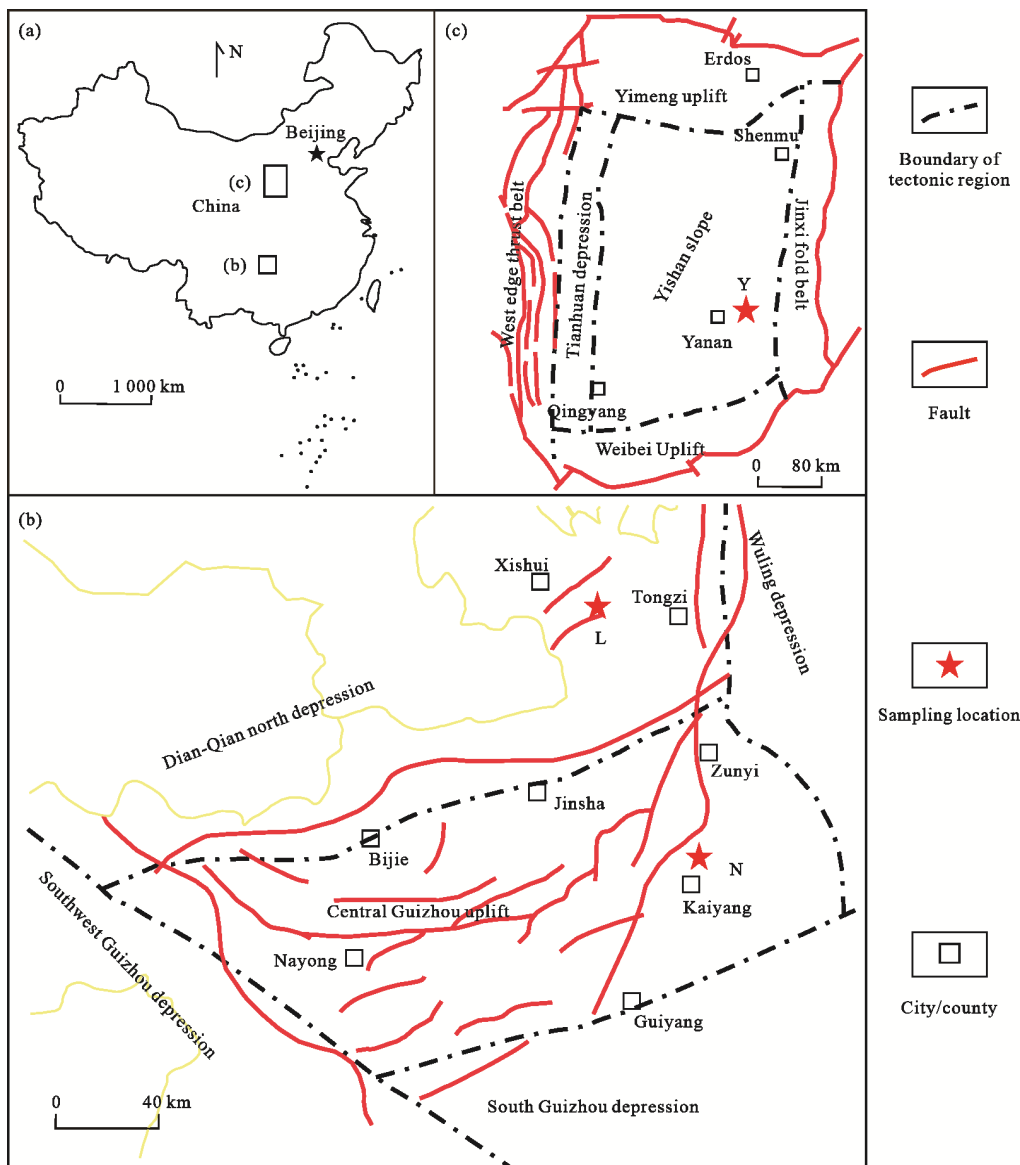


**Figure 1.** Sketch maps showing the regional geology and sampling sites. (a) Sketch map showing the locations of research area (b) and (c) (map of China after GS(2016)1555); (b) northern Guizhou and the compositional tectonic units, in which Longmaxi samples from outcrop section (sampling site L) in the eastern of Dian-Qian north depression; and Niutitang samples from ZK 105 (sampling site N) in the east of the Central Guizhou uplift; (c) locations of Ordos Basin and the compositional tectonic units, in which Yanchang samples collected from Well #941 (sampling site Y) located in the eastern edge of the Yishan slope.

## 2 SAMPLES AND METHODS

### 2.1 Samples

A total of 15 Yanchang core samples (Y-1 to Y-15) were collected from Well #941 in Ordos Basin, China (sampling site Y, Fig. 1c), ranging from 692 to 718 m in depth in the Chang 7 member (Fig. 2). The Longmaxi outcrop samples were drilled by a Shaw portable core drilling equipment at a site in Xishui, Guizhou Province (sampling site L, Fig. 1b). The Longmaxi shales at the sampling site L are divided into three members, in which Long 1 member is the best source rock and further divided into 9 layers; 15 samples (L-1 to L-15) were collected from the 1<sup>st</sup> to 9<sup>th</sup> layers in the Long 1 member (Fig. 2). The Niutitang shale samples were obtained from well ZK 105 in Kaiyang, Guizhou Province (sampling site N, Fig. 1b). Fourteen core samples (N-1 to N-14) were collected every several meters from top to bottom within an interval of 60 m (Fig. 2). All 44

samples were analyzed for TOC contents,  $R_o$ , and mineralogical composition, and 15 samples (five samples from each formation) were selected to conduct FE-SEM observations. Based on the above analyses, HR-TEM were conducted on nanocomposites in three representative samples (Y-14, L-13, N-12) from these three different formations with various maturities.

### 2.2 Organic Geochemical Analyses

The TOC contents were measured using an elemental analyzer designed for organic matter analyses (Vario MACRO Cube), following the Chinese Oil and Gas Industry Standard GB/T 19145-2003 (General Administration of Quality Supervision, Inspection and Quarantine of the People's Republic of China, 2003). The inorganic carbon was removed by the acid digestion with dilute hydrochloric acid before the measurement.

Laser Raman spectroscopy has been proven to be an effec-

tive method to calculate vitrinite reflectance (Chen et al., 2015; Tuschel, 2013; Kelemen and Fang, 2001). The reflectance values ( $R$ ) of OM (vitrinite for Yanchang shale and bitumen for Longmaxi and Niutitang shales) were calculated from laser Raman spectra acquired using a Renishaw Invia Reflex Laser Raman Spectrometer (wavenumbers ranging from 100 to 4 000  $\text{cm}^{-1}$ ) using the equation described by Liu et al. (2012)

$$R = 0.0537 d(G-D) - 11.21 \quad (2-1)$$

where  $G$  and  $D$  denote the peak positions of graphitic carbon and disordered carbon, respectively, and  $(G-D)$  is the interpeak interval between the  $G$  and  $D$  bands (Liu et al., 2012; Kelemen and Fang, 2001). This equation has been reported as an applicable calculation for maturity (Chen et al., 2015). For Yanchang samples, the  $R$  represents vitrinite reflectance (equivalent  $R_o$  in Fig. 2). For Longmaxi and Niutitang samples, thermal maturity was measured using bitumen reflectance ( $R_b$ ), since vitrinite is absent in these Lower Paleozoic marine shales.  $R_b$  was then converted to  $R_o$  (i.e., equivalent  $R_o$  in Fig. 2) using the relationship for highly overmature samples published by Schoenherr et al. (2007)

$$R_o = (R_b + 0.2443)/1.0495 \quad (2-2)$$

### 2.3 X-Ray Diffraction (XRD)

The mineralogical composition of the samples was determined using a Bruker D8 ADVANCE X-ray diffractometer with a testing angle ranging from  $5^\circ$  to  $90^\circ$ . The samples were crushed and ground to be finer than 200 mesh. The analyses of clay minerals followed the Chinese Oil and Gas Industry Standard SY/T 5163-2010 (National Energy Administration, 2010).

### 2.4 Field Emission-Scanning Electron Microscopy (FE-SEM)

Before SEM observations, a Leica EM TIC 3X argon ion polisher was used to polish the sample surface, which was then coated with gold to obtain an electrically conductive surface. The secondary electron images were captured to characterize the morphology and structure of samples, using an acceleration voltage of 20 kV, with a FEI Scios FE-SEM at the Institute of Geochemistry, Chinese Academy of Sciences.

### 2.5 High Resolution-Transmission Electron Microscopy (HR-TEM)

To acquire more refined structural characteristics, the HR-TEM imaging with energy dispersive spectroscopy (EDS) was conducted on nanocomposites. To find the precise objective, the FIB-SEM instrument (FEI Scios) with EDS was used to search for nanocomposites in three samples and prepare ultra-thin sections by integrating nanoscale cutting with a gallium ion beam. Then ultra-thin sections, approximately 80 nm thick, were prepared for the HR-TEM analysis, which was carried out on a FEI Tecnai G<sup>2</sup> F20 at the Institute of Geochemistry at Chinese Academy of Sciences.

## 3 RESULTS AND DISCUSSION

### 3.1 Sample Composition

Figure 2 illustrates the sampling location, depth, TOC,  $R_o$  and mineralogical composition of a total of 44 samples. The

TOC contents range from 0.43% to 3.84% for Yanchang samples (TOCs of most samples  $>2.0\%$ ), from 0.37% to 5.48% for Longmaxi samples, from 0.33% to 5.52% for Niutitang samples with average values of 2.67%, 2.63%, and 2.20%, respectively. Therefore, most samples can be described as having good present-day TOC contents. The equivalent  $R_o$  values vary from 0.71% to 1.41% for Yanchang samples, from 2.56% to 2.91% for Longmaxi samples, and from 2.86% to 3.32% for Niutitang samples, with averages of 1.04%, 2.79%, and 3.06%, respectively. The ranges of equivalent  $R_o$  for three formations are consistent with previous studies (Wang et al., 2016; Guo et al., 2014), representing the thermal evolutionary process from oil-window mature to overmature.

In terms of mineralogical composition, these 44 samples are mainly composed of quartz, clay and feldspars, with low carbonate mineral contents (Fig. 2). Overall, the quartz contents of the samples from Longmaxi and Niutitang shales (averaged at 46% and 44%, respectively) are significantly higher than that of Yanchang samples (30%), while the feldspar contents (averages of 17% and 15%) are significantly lower than that of Yanchang samples (29%). Samples from Longmaxi shale have lower clay contents (average 29%) than those from Yanchang and Niutitang shales (averages of 37% and 35%), higher carbonate contents (averages of Longmaxi, Niutitang, Yanchang samples are 6%, 3%, and 2%, respectively). The different mineral composition of three shales indicates that Longmaxi and Niutitang shales have a better friability (and stronger fracability) than Yanchang shale.

### 3.2 Structural Characteristics Based on SEM Observations

The OM is present in different forms in the studied samples as observed under SEM (Figs. 3–5): particulate OM and clay-organic nanocomposites. The OM particles commonly appear as irregular forms and have a clear boundary with surrounding minerals, whereas the nanocomposites present an alternative arrangement of OM (light gray) and clay minerals (dark gray), indicating a close relation between OM and clays in these samples. The wide distribution of nanocomposites in these three shales demonstrates the importance of nanocomposites for OM occurrence, highlighting the contribution of nanocomposites to petroleum generation (Zhu et al., 2018). The yellow-dotted curves in Figs. 3–5 present the morphological distribution of nanocomposites. In general, clay minerals in source rocks appear as band-like stacks through the sedimentation and diagenesis processes. For the lacustrine shale (Yanchang), as shown in Fig. 3, most nanocomposites have the characteristics of sub-parallel bands. Some brittle minerals (such as quartz) are also mixed with the nanocomposites (Figs. 3b and 3f), which indicates the interference of terrigenous/authigenic materials on the nanocomposites during sedimentation or diagenesis. For the Longmaxi (Fig. 4) and Niutitang shales (Fig. 5), OM and clay minerals in nanocomposites behave as obvious layered distribution accompanied by pyrite nanoparticles which are extensively distributed between clay layers, suggesting an anoxic and reducing environment of deposition. In addition, the clay minerals in part of nanocomposites behave as card-house structure (Figs. 4c and 5c), which is built-up by the edge (+)/face (-) contacts between clay layers

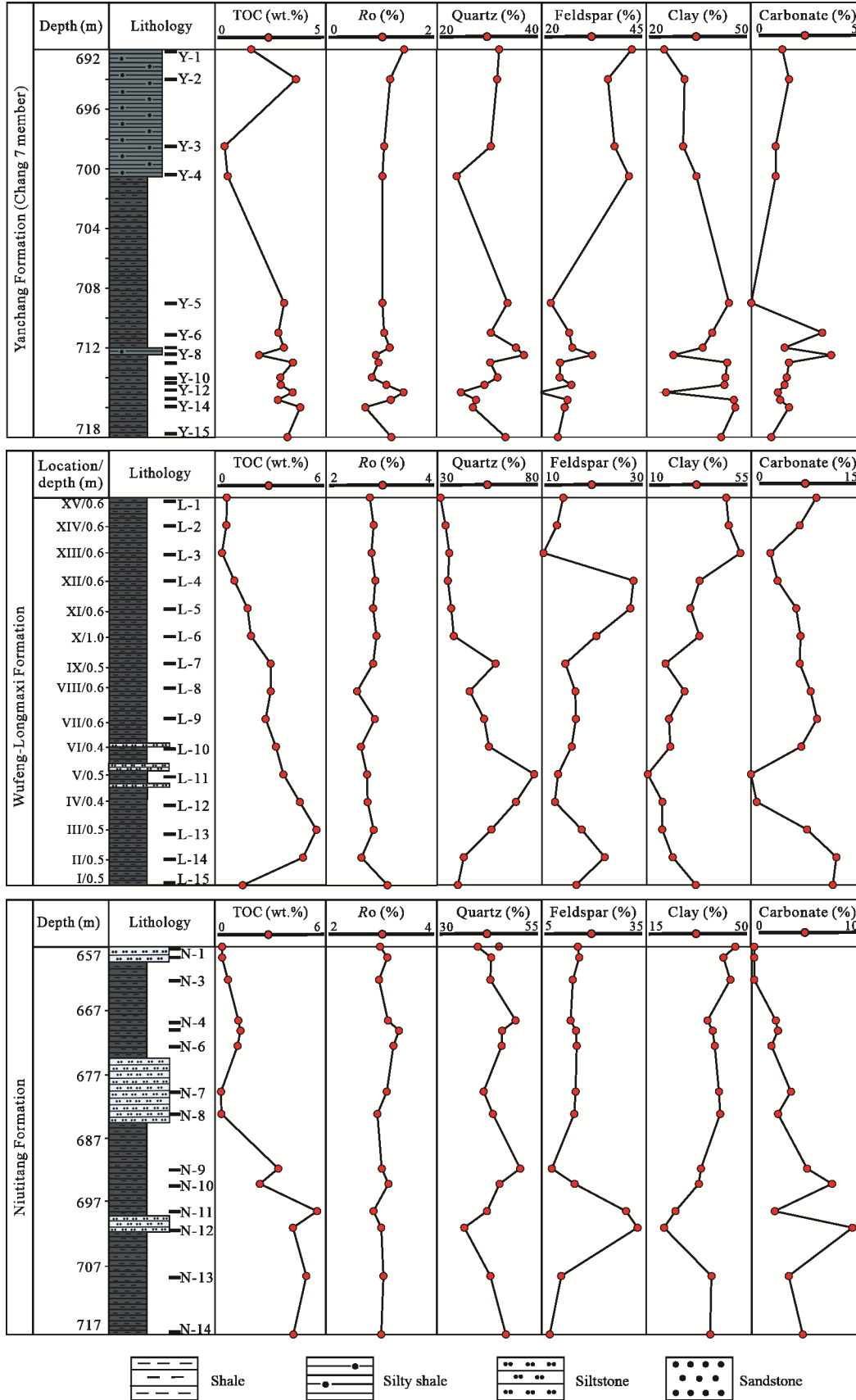


**Figure 2.** Diagrams showing the sampling location, lithology, and composition characteristics of three formations. (a) Yanchang Formation (Chang 7 member); (b) Wufeng-Longmaxi Formation; (c) Niutitang Formation. Locations: I. 1<sup>st</sup> layer; II. lower 2<sup>nd</sup> layer; III. upper 2<sup>nd</sup> layer; IV. lower 3<sup>rd</sup> layer; V. upper 3<sup>rd</sup> layer; VI. lower 4<sup>th</sup> layer; VII. upper 4<sup>th</sup> layer; VIII. lower 5<sup>th</sup> layer; IX. upper 5<sup>th</sup> layer; X. 6<sup>th</sup> layer; XI. 7<sup>th</sup> layer; XII. lower 8<sup>th</sup> layer; XIII. upper 8<sup>th</sup> layer; XIV. lower 9<sup>th</sup> layer; XV. upper 9<sup>th</sup> layer.

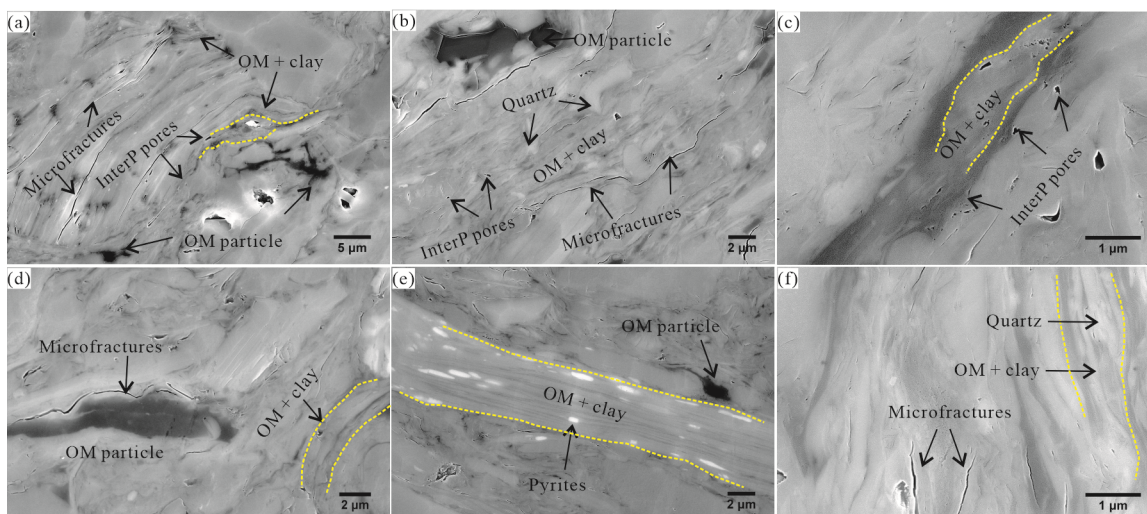


**Figure 3.** FE-SEM images from secondary electron detections of Yanchang samples, with the yellow-dotted curves denoting the presence of nanocomposites. Sub-parallel bands nanocomposites are found in all images and often accompanied by OM particles in (a)–(b) and (d)–(f), and partial nanocomposites are mixed with quartz particles in (b) and (f), along with interparticle pores in (a)–(c) and microfractures in (a)–(b) and (d)–(f).

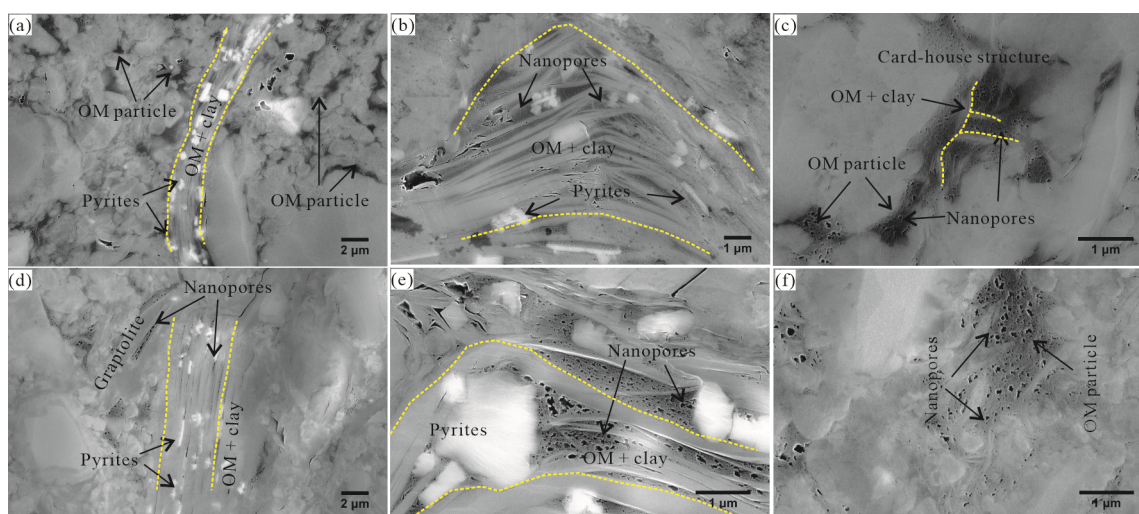


**Figure 4.** FE-SEM images from secondary electron detections of Longmaxi samples with yellow-dotted nanocomposites, illustrating the OM particles and the nanopores in OM (a), (c), and (f), abundant nanopores in nanocomposites (b)–(e); the nanocomposites in (a)–(b) and (d)–(e) present obvious layered distribution accompanied by pyrite particles, while (c) shows the feature of card-house nanocomposites.

and preserved by passive pore filling (probably as biological fossils), before the clay layers were significantly compacted (Liu et al., 2019; Day-Stirrat et al., 2008; Lagaly, 1989; O'Brien, 1971). Most nanocomposites have suffered a deformation to be changed to various shapes, such as triangular (Figs. 4b and 4e), lenticular (Fig. 5e), as well as irregular (Figs. 3a, 3d, 5b). The plastic nature of clay networks and OM provide an opportunity for the secondary change of nanocomposites' morphology after sedimentation. Then the stress, probably derived from mineral particles (such as pyrites in Figs. 4b, 4e, and 5b) and geostress (such as shear stress in Fig. 5e), causes the original composites to be deformed to various shapes.

Another significant difference between three formations is the development of nanometer-sized pores. For Yanchang samples with an equivalent  $R_o \sim 1\%$ , OM pores are rarely developed, and interparticle mineral pores and microfractures occasionally appear within or around nanocomposites (Fig. 3).

While in Longmaxi samples with a higher equivalent  $R_o \sim 2.8\%$ , OM pores with different shapes and diameters ranging from several to hundreds of nanometers are widely distributed in the particulate OM, which is identical with previous studies (Fu et al., 2022; Wang Z M et al., 2022; Wang P F et al., 2016), and similarly-sized pores are ubiquitous in the nanocomposites (Fig. 4). Compared to Longmaxi samples (type I kerogen), undeveloped OM pores in Yanchang samples are likely related to the low petroleum generation potential of OM types (type II and type III) at low mature stage (Gu et al., 2021a). However, Niutitang samples at the highest equivalent  $R_o \sim 3\%$  show large amounts of non-porous OM particles (Figs. 5a and 5d) as a consequence of complete gas expulsion (and pore collapse) attributed to the development of microfractures and framework compaction (Liu et al., 2016; Milliken et al., 2013). In addition, the differences of nanopore development in nanocomposites among these three shales could be related to various fac-

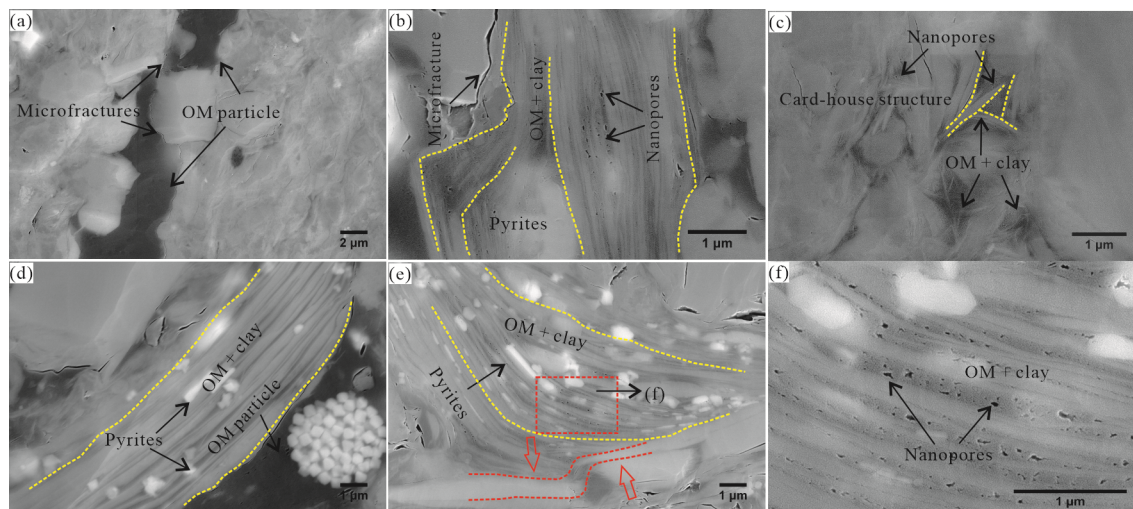


**Figure 5.** FE-SEM images from secondary electron detections of Niutitang samples, with the yellow-dotted curves denoting the presence of nanocomposites, and the red-dotted curves and arrows indicating the deformation and shear stress direction in (e). (a)–(b) present the microfractures around OM particles and nanocomposites, respectively; and (c)–(e) show the card-house, band-like, and deformed nanocomposites, respectively. The nanopores are extensively distributed in (b)–(c) and (e)–(f), and pyrite particles are also common in the nanocomposites in (b) and (d)–(f).

tors, including thermal maturity, OM type, clay minerals and burial history (Gu et al., 2021a; Curtis et al., 2012; Loucks et al., 2009). For example, the abundant porous nanocomposites and nonporous OM particles in Niutitang samples (Figs. 5b, 5c, and 5f) suggest the protection of nanopores by clay layers, which are reported in a previous study of Gu et al. (2021b).

### 3.3 Structural Characteristics Based on XRD and TEM Results

To explore the structural characteristics of nanocomposites in more detail, three samples (Y-14, L-13, and N-12) from different formations and maturities were selected for XRD and TEM analyses. The XRD data of these three samples are presented in Fig. 6, with quartz, clays, calcite, feldspar, and pyrite as the dominant minerals. Clay minerals in the Yanchang sample (Y-14) were identified as illite, smectite, mixed-layer illite/smectite (I/S), and kaolinite. Illite or mixed-layer I/S and kaolinite dominate the clay components in the Longmaxi (L-13) and Niutitang (N-12) samples. According to the Chinese Standard SY/T 5163-2010 (National Energy Administration, 2010), a sharper peak shape of illite or mixed-layer I/S ( $2\theta = 9.1^\circ$ ) in Fig. 6 represents a higher degree of order. The full width at half maximum (FWHM) is used to characterize the sharpness of peak, and the smaller FWHM, the higher ordered degree. The FWHM of the peak ( $2\theta = 9.1^\circ$ ) for three samples (Y-14, L-13, N-12) are 0.151, 0.251, and 0.227, respectively. For Sample Y-14, considering the presence of diffraction peak for smectite and the low maturity (illitization process has just started to occur), the minimum FWHM may represent relatively pure illite (high ordered degree), which was likely originated from primary sediment rather than illitization of smectite. However, a non-noticeable diffraction peak for smectite in samples L-13 and N-12 and larger FWHMs indicates the presence of mixed-layer I/S from the smectite illitization. In addition, mixed-layer I/S in Sample N-12 has the higher ordered degree (smaller FWHM) than Sample L-13, implying that thermal evolution

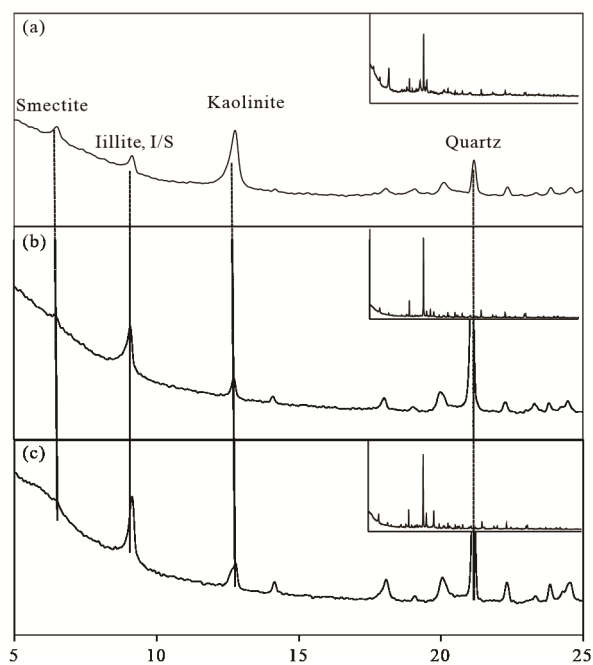


**Figure 6.** XRD spectra of three powdered samples; I/S, mixed-layer illite/smectite; (a), (b), and (c) represent the samples of Y-14, L-13, and N-12, respectively.

drives the illitization of smectite. In a brief summary, thermal evolution could alter clay composition and affect the transformation of clay minerals.

As shown in the left panel of Fig. S1, typical nanocomposites for three samples were selected for slicing in approximately  $10\ \mu\text{m} \times 10\ \mu\text{m}$  sections with FIB-SEM. The secondary electron images of three sections can be seen in the right panel of Fig. S1, from which, it can be identified that organic carbon (dark color) is distributed between clay layers (grey). In addition, the clay-organic nanocomposites in these three sections extend tens of microns in the direction parallel to bedding (the

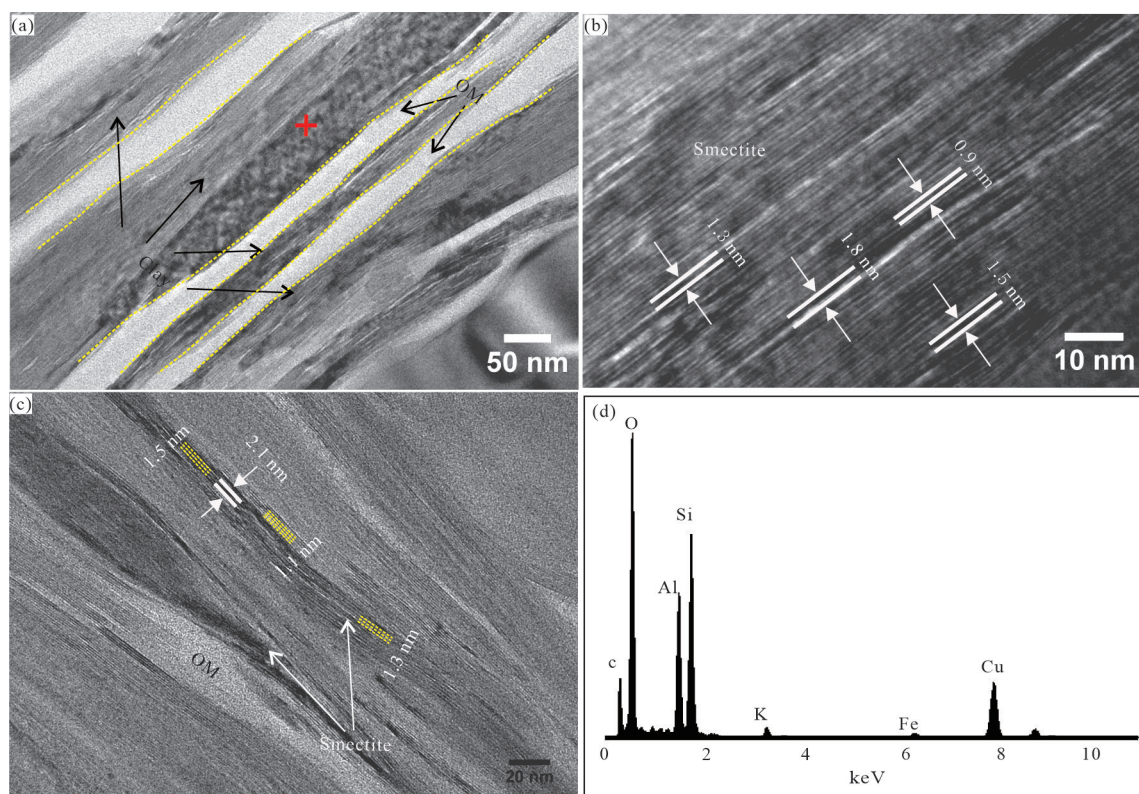


**Figure 7.** Structural characteristics of nanocomposites in Sample Y-14 from HR-TEM. (a) Distribution of clay and OM (yellow-dotted curves denote the boundary between clay layers and OM); (b)–(c) the differences in the ‘*d*’ value (as shown by white solid lines and yellow-dotted lines), meaning the expansivity of clay layers (smectite); (d) the EDS spectrum of the red cross in (a). The light gray denotes OM, while dark gray clays.

white-dotted lines in the right panel of Fig. S1), indicating the bedding distribution of nanocomposites. The plastic deformation seems to be universal in the nanocomposites, probably resulting from the reservoir stress and plasticity of clay layers.

To confirm OM occurrence in the three samples studied, the bright field of HR-TEM was utilized for detailed observations. As shown in Fig. 7a, the clays in Sample Y-14, which are dark grey and composed of multi-layers of clay (smectite or illite), are interbedded with OM (light grey and amorphous). These phyllosilicates are also widely recognized within samples L-13 (Figs. 8a–8b) and N-12 (Fig. 9a). According to the EDS results of a point in the clay-rich parts for each of three samples (Figs. 7d, 8f, and 9d), the carbon peak is noticeable for Sample Y-14, and negligible for samples L-13 and N-12. The magnification of clay-rich areas shows that the clays consist of tens of monolayers, which are about 1–2 nm thick (Figs. 7b–7c, 8c–8e, and 9b–9c). Therefore, these areas are multi-layers of clays at several to tens of nanometers in thickness. More notably, the monolayer thickness is not always consistent. Mostly two values are found for the monolayer thickness of clay (‘*d*’ value): approximately 1.5 and 1.0 nm, representing the monolayer thickness of smectite and illite (Li et al., 2020; Środoń, 2006).

For Sample Y-14, the multi-layers of clay consist mainly of smectite, which exhibits a remarkable range of ‘*d*’ values (from 0.9 to 2.1 nm) (Figs. 7b–7c). Combined with the EDS analyses, a certain amount of organic carbon is distributed in clay layers (Fig. 7d). It is reasonable to expect that the organic carbon has occupied the interlayer space of smectite, resulting

in the expansion of interlayer. For Sample L-13, several mixed-layer I/S were photographed, and the conjugation site between smectite and illite (yellow box in Fig. 8c) shows a different ‘*d*’ value (1.7 nm) compared with smectite or illite, suggesting the structural transformation of clay layers during smectite illitization. For Sample N-12, most of the clay layers are identified as illite, demonstrated by a stable ‘*d*’ value of 1.0 nm (Figs. 9b–9c). The distributions of smectite and illite observed from the TEM images of three samples are quite consistent with the peak shapes of illite or mixed-layer I/S in XRD analyses (Fig. 6). In addition, the pyrite nanoparticles, observed by SEM imaging to be extensively distributed between clay layers and co-existing with organic carbon for samples L-13 and N-12, could impose a stress on clays and cause the deformation of clay layers (Figs. 8a and 9a).

### 3.4 Evolution of Clay-Organic Nanocomposites in Shale

Considering that petroleum generation from OM and the structure of clay minerals are regulated by maturity to a certain extent (Bu et al., 2017; Berthonneau et al., 2016; Kennedy et al., 2014), the structure and component transformation of clay-organic nanocomposites are explored from the perspective of thermal evolution. In this study, the layer structures of clay minerals in nanocomposites from oil window to over-maturity provide insights into the evolution of nanocomposites. Previous studies have shown the existence of organic carbon in internal surfaces of clays (Zhu H J et al., 2020; Berthonneau et al., 2016; Zhu X J et al., 2016). In the present work, the carbon



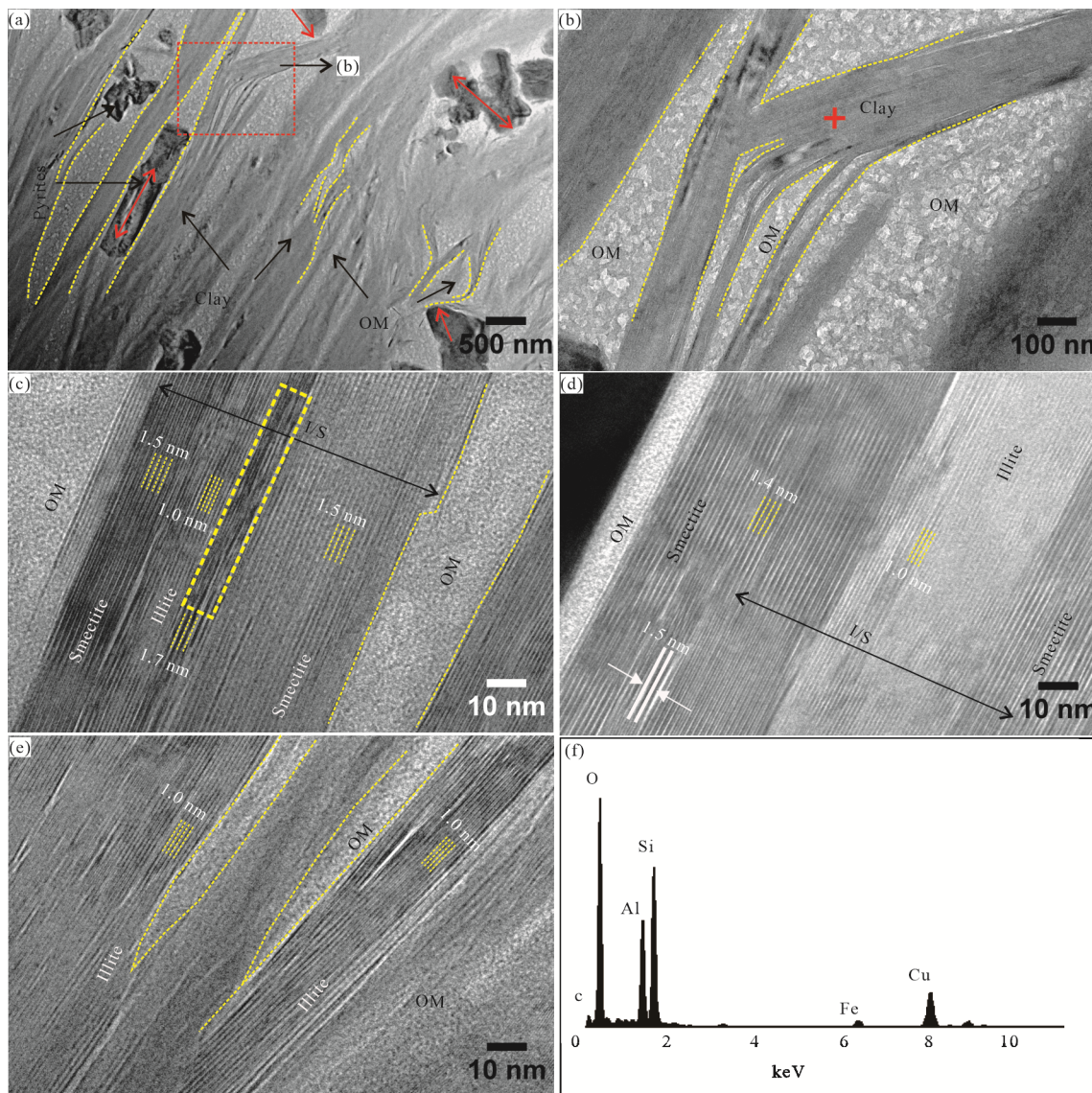


**Figure 8.** Structural characteristics of nanocomposites in Sample L-13 from HR-TEM. (a), (b), (e) Distribution of clay and OM, and (c), (d) the mixed-layer I/S ( $d$  value alternates between 1.4/1.5 nm (smectite) and 1.0 nm (illite), as shown by yellow-dotted lines). (e) More ordered illite layers, and F illustrates the EDS spectra of the corresponding mark points in (b) (red cross). The red arrows denote the imposed stress of pyrites on clay, and the yellow box in (c) denotes the conjugation site between smectite and illite.

peak arising in EDS spectra for corresponding clay layers in Sample Y-14 also confirms that organic molecules are likely to be present in the interlayer space (Fig. 7). The large differences in monolayer thickness (from 0.9 to 2.1 nm) (Figs. 7b–7c) also provide circumstantial evidence for the presence of organic molecules in the interlayer space of expandable clays (smectite). Since the expandable nature of smectite interlayers, organic molecules could access the interlayer sites of smectite, and enlarge the interlayer spacing (Bu et al., 2017; Chen et al., 2008; Jia et al., 2002; Sposito et al., 1999; Theng et al., 1986), and this has been hypothesized to protect organic carbon from microbial degradation or oxidation in the water column during early diagenesis (Kennedy and Wagner, 2011; Kennedy et al., 2002). The illitization of smectite then occurs during thermal evolution (Berthonneau et al., 2016; Metwally and Chesnokov, 2012; Lanson et al., 2009; Hower et al., 1976), as illustrated by the decreasing  $d$  value (from 1.5/1.4 to 1.0 nm) (Figs. 8c–

8d). The transformation of clay minerals during thermal evolution is an important driver to change the composition of mudstone (Aplin and MacQuaker, 2011). The occurrence of the mixed-layer I/S in Longmaxi samples (Figs. 8c–8d), featuring an isomorphous substitution occurring in the tetrahedral sheets (Si by Al) (Berthonneau et al., 2016), also suggests the illitization of smectite. The peak shapes of illite or mixed-layer I/S in Figs. 6a–6c also present an increasing order of mixed-layer I/S with increasing maturity. Significantly, the fluctuations of clay interlayer spacing become less distinctive with increasing maturity (from Fig. 7 to Fig. 9), representing an increasing illitization and the migration of organic molecules (through gaseous hydrocarbon generation) from interlayer spaces (Du et al., 2021; Berthonneau et al., 2016), leading to a formation of stable nanocomposites (Figs. 9e–9f).

It is found that the interlayer spaces could be divided into multi-layer spaces (the space between two clay crystals), often

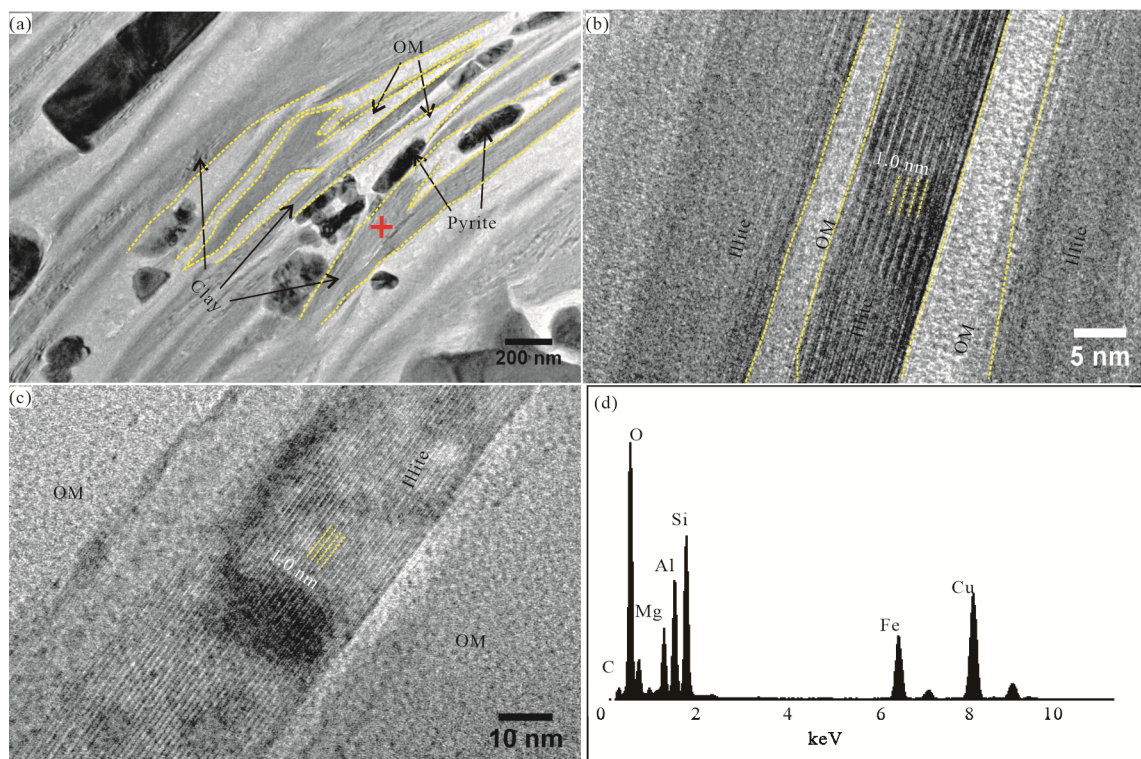


**Figure 9.** Structural characteristics of nanocomposites in Sample N-12 from HR-TEM. (a) Distribution of clay and OM; and (b), (c) stable 'd' value (1.0 nm) of illite (as shown by yellow-dotted lines), implying the in-expansibility of illite; (d) the EDS spectra of the point marked by a red cross in (a).

occupied by OM and pyrite (as shown in Figs. 7a, 8a–8b, and 9a–9b), and monolayer spaces of clay (expandable space in smectite as shown in Fig. 7b and stable space in illite in Figs. 8e and 9b–9c). The elemental mapping in the area of Fig. 8a represents the distribution of clay, organic carbon, and pyrite (Fig. S2), indicating that large amounts of organic carbon is preferentially associated with the spaces between multi-layers of clay. The organic carbon between monolayers of clay is only detected in Yanchang sample (Fig. 7), but not detected in the Longmaxi and Niutitang samples (Figs. 8f and 9d). This fraction of organic carbon makes up much less proportion in the three samples than that in multi-layer spaces (Figs. 7a, 7c, 8b, 8c, 8e, 9a, 9b). This distribution characteristic proves that the organic carbon between multi-layers should dominate the occurrence of OM in nanocomposites, which is a significant extension for the traditional opinions of OM-clay association (i.e., organic carbon distributed abundantly in the interlayer (monolayer) spaces of clay) (Zhu et al., 2016; Kennedy et al., 2014). In addition, the clay multi-layers are always non-parallel to each other (as shown by the yellow-dotted curves in Figs. 7c, 8b, 8e, and 9a), which could be caused by the incorporation of OM distributed in the space between multi-layers. Therefore, we suggest that the OM in multi-layer spaces is not native to the surrounding clays, but trapped in the interlayer spaces along the weak plane of clays during maturation, and these parts of OM are likely to be the source of organic molecules in the space between monolayers.

The clay-OM association can give insights into the organic-inorganic synergies involved in the sequestration and preservation, as well as petroleum generation of OM during burial

(Zhu et al., 2018; Berthonneau et al., 2016; Kennedy et al., 2014). Intrinsically, the deposition of OM is a slow process as its density is fairly close to water. However, adsorption onto denser particles (such as minerals) could accelerate the process (Berthonneau et al., 2016). The water in clays may be replaced by organic molecules, resulting in the OM being adsorbed at clay surfaces or trapped in the interlayer space (Berthonneau et al., 2016; Tosca et al., 2010; Kennedy et al., 2006). Then the diagenesis process promotes the evolution of clay minerals and OM. By integrating the above studies, the evolution of nanocomposites can be divided into following four stages (as shown in Fig. 10): (1) OM is adsorbed onto clay particles in the water column, which provides the basis for the formation of nanocomposites (Berthonneau et al., 2016). Then during early diagenesis, OM trapped in the multi-layer space along weak stress surface or adsorbed on the surface and edge of clay. (2) Thermal maturation provokes organic molecules (probably derived from the organic carbon trapped in the multi-layer space) inserting into the monolayer space, and promotes petroleum generation from the OM and mineral transformation (illitization of smectite) (Figs. 7b, 7c). (3) Then with increasing maturity, the organic molecules migrate from monolayer spaces through generating gaseous hydrocarbons, and mixed-layer I/S formed (Figs. 8c, 8d). (4) Finally, the mineral transformation is completed (Figs. 8e, 9b, 9c), accompanied by the formation of final nanocomposites comprising of stable clay layers and remaining organic carbon between multi-layer spaces.

#### 4 CONCLUSIONS

In this research, a total of 44 samples of organic matter-rich

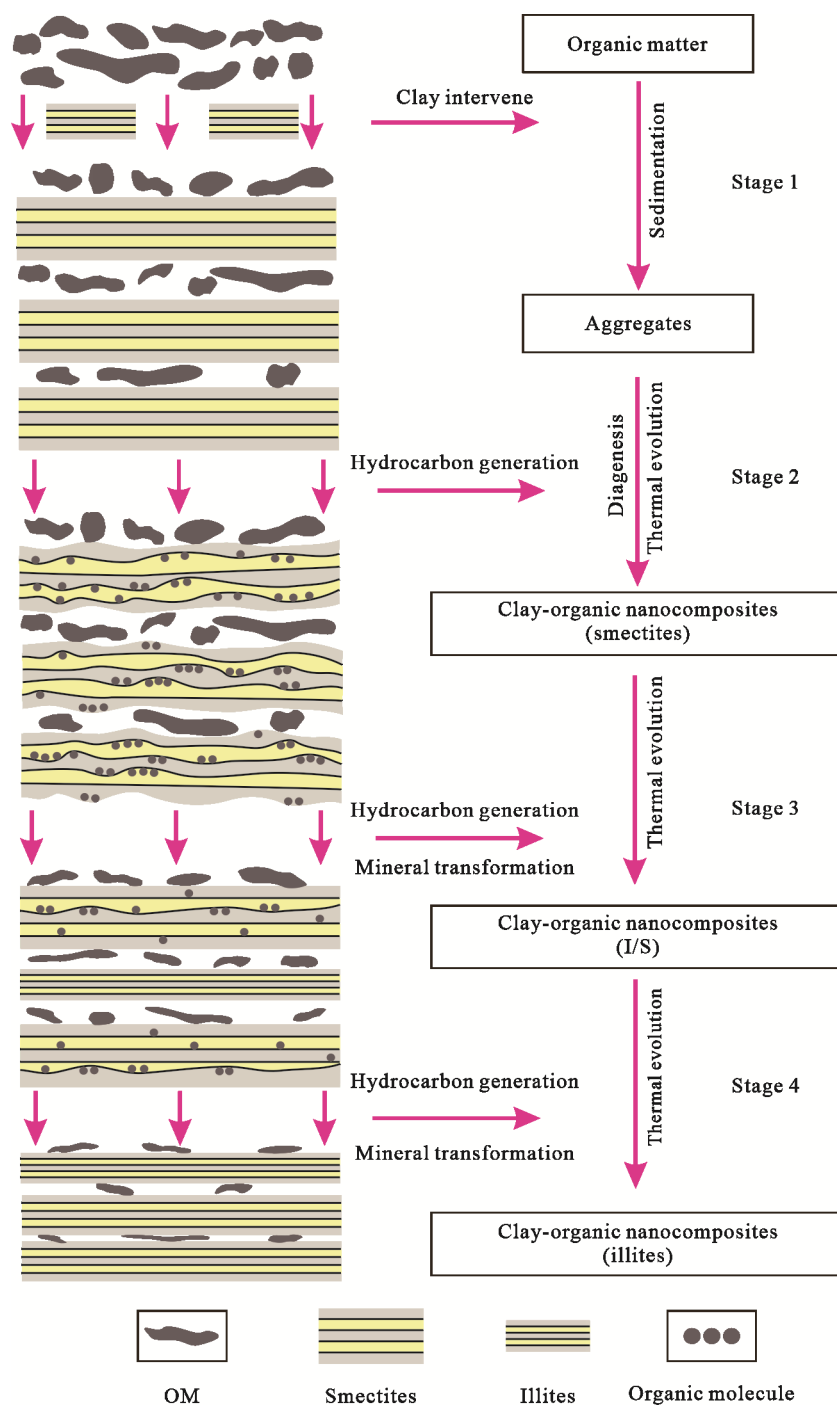


Figure 10. A schematic diagram for the evolution process of clay-organic nanocomposites in shale.

source rocks (15 lacustrine shale samples from Yanchang, 15 marine shale samples from Longmaxi, and 14 marine shale samples from Niutitang) in China were collected to characterize the structure, and specify the evolution, of clay-organic nanocomposites. The equivalent  $R_o$  values of these formations are 1.0%, 2.8%, and 3.1% on average, representing oil-window and dry gas to overmature sediments. OM occurrence within the studied shales occurs as either discrete particles or clay-organic nanocomposites, which have different structural features among three formations, including the morphology, nanopore development, and occurrence of the OM. For Yanchang shale, sub-parallel bands and intermingling with brittle minerals (such as

quartz) are the principal forms of nanocomposites, with inter-particle mineral pores randomly developed around the nanocomposites. For Longmaxi and Niutitang shales, layered distributions of OM and clay minerals, and abundant nanopores dominate the features of nanocomposites, accompanied by pyrite nanoparticles extensively distributed between clay layers, suggesting an anoxic and reducing environment of deposition. In addition, most nanocomposites present various deformed characteristics, probably caused by mineral particles and geostress.

The presence of OM between multi-layer spaces and monolayer spaces of clays have been confirmed by integrated analyses, and the distribution of OM in nanocomposites and

their structures are different in these three leading shales in China. OM mainly occur between the multi-layer spaces of clay, proving that the organic carbon between multi-layers dominate the OM occurrence in nanocomposites, which is an important extension for the traditional opinion of OM-clay association. The OM between monolayer of clays is only detected for Yanchang shale at low maturation stage, implying that the organic molecules have migrated from monolayer spaces as gaseous hydrocarbons are generated with increasing maturity. With the evolutional process of nanocomposites in shale, petroleum generation from OM and structural transformation as well as reorganization of clay frameworks (e.g., illitization of smectite) run in parallel, which also stabilizes nanocomposites. Then the nanocomposites, comprising of stable clay layers and remaining organic carbon between multi-layer spaces, are formed at overmature stage. This evolution process of nanocomposites would definitely illustrate the changes in the structure of clay, and improve the understanding of petroleum generation and organic-inorganic interactions.

#### ACKNOWLEDGMENTS

This study was funded by the National Natural Science Foundation of China (Nos. 41802143, 41690134, and 41821002), the Open Foundation of the State Key Laboratory of Ore Deposit Geochemistry in China (No. 201904), and the Natural Science Foundation of Henan Province (No. 212300410129). We greatly thank three anonymous reviewers and the editors who provided valuable comments to improve the quality of this work. The final publication is available at Springer via <https://doi.org/10.1007/s12583-022-1717-y>.

**Electronic Supplementary Materials:** Supplementary materials (Figs. S1–S2) are available in the online version of this article at <https://doi.org/10.1007/s12583-022-1717-y>.

#### REFERENCES CITED

- Aplin, A. C., Bishop, A. N., Clayton, C. J., et al., 1992. A Lamina-Scale Geochemical and Sedimentological Study of Sediments from the Peru Margin (Site 680, ODP Leg 112). *Geological Society, London, Special Publications*, 64(1): 131–149. <https://doi.org/10.1144/gsl.sp.1992.064.01.0>
- Aplin, A. C., MacQuaker, J. H. S., 2011. Mudstone Diversity: Origin and Implications for Source, Seal, and Reservoir Properties in Petroleum Systems. *AAPG Bulletin*, 95(12): 2031–2059. <https://doi.org/10.1306/03281110162>
- Berthonneau, J., Grauby, O., Abuhaikal, M., et al., 2016. Evolution of Organo-Clay Composites with Respect to Thermal Maturity in Type II Organic-Rich Source Rocks. *Geochimica et Cosmochimica Acta*, 195: 68–83. <https://doi.org/10.1016/j.gca.2016.09.008>
- Bu, H. L., Yuan, P., Liu, H., et al., 2017. Effects of Complexation between Organic Matter (OM) and Clay Mineral on OM Pyrolysis. *Geochimica et Cosmochimica Acta*, 212: 1–15. <https://doi.org/10.1016/j.gca.2017.04.045>
- Cai, J. G., Bao, Y. J., Yang, S. Y., et al., 2007. Research on Preservation and Enrichment Mechanisms of Organic Matter in Muddy Sediment and Mudstone. *Science in China Series D: Earth Sciences*, 50(5): 765–775. <https://doi.org/10.1007/s11430-007-0005-0>
- Cai, J. G., Song, M. S., Lu, L. F., et al., 2013. Organo-Clay Complexes in Source Rocks—A Natural Material for Hydrocarbon Generation. *Marine Geology & Quaternary Geology*, 33(3): 123–131 (in Chinese with English Abstract)
- Cai, J. G., Zhu, X. J., Zhang, J. Q., et al., 2020. Heterogeneities of Organic Matter and Its Occurrence Forms in Mudrocks: Evidence from Comparisons of Palynofacies. *Marine and Petroleum Geology*, 111: 21–32. <https://doi.org/10.1016/j.marpetgeo.2019.08.004>
- Cao, H. Y., Zhu, C. Q., Qiu, N. S., 2015. Thermal Evolution of Lower Silurian Longmaxi Formation in the Eastern Sichuan Basin. *Journal of Earth Sciences and Environment*, 37(6): 22–32 (in Chinese with English Abstract)
- Chen, G. J., Yen, M. C., Wang, J. M., et al., 2008. Layered Inorganic/Enzyme Nanohybrids with Selectivity and Structural Stability upon Interacting with Biomolecules. *Bioconjugate Chemistry*, 19(1): 138–144. <https://doi.org/10.1021/bc700224q>
- Chen, S. B., Zuo, Z. X., Zhu, Y. M., et al., 2015. Applicability of the Testing Method for the Maturity of Organic Matter in Shale Gas Reservoirs. *Natural Gas Geoscience*, 26(3): 564–574 (in Chinese with English Abstract)
- Curtis, M. E., Cardott, B. J., Sondergeld, C. H., et al., 2012. Development of Organic Porosity in the Woodford Shale with Increasing Thermal Maturity. *International Journal of Coal Geology*, 103: 26–31. <https://doi.org/10.1016/j.coal.2012.08.004>
- Dai, J. X., Li, J., Luo, X., et al., 2005. Stable Carbon Isotope Compositions and Source Rock Geochemistry of the Giant Gas Accumulations in the Ordos Basin, China. *Organic Geochemistry*, 36(12): 1617–1635. <https://doi.org/10.1016/j.orggeochem.2005.08.017>
- Day-Stirrat, R. J., Loucks, R. G., Milliken, K. L., et al., 2008. Phyllosilicate Orientation Demonstrates Early Timing of Compactional Stabilization in Calcite-Cemented Concretions in the Barnett Shale (Late Mississippian), Fort Worth Basin, Texas (USA). *Sedimentary Geology*, 208(1/2): 27–35. <https://doi.org/10.1016/j.sedgeo.2008.04.007>
- Dong, D. Z., Wang, Y. M., Li, X. J., et al., 2016. Breakthrough and Prospect of Shale Gas Exploration and Development in China. *Natural Gas Industry*, 36(1): 19–32 (in Chinese with English Abstract)
- Du, J. Z., Cai, J. G., Lei, T. Z., et al., 2021. Diversified Roles of Mineral Transformation in Controlling Hydrocarbon Generation Process, Mechanism, and Pattern. *Geoscience Frontiers*, 12(2): 725–736. <https://doi.org/10.1016/j.gsf.2020.08.009>
- Duan, Y., Wang, C. Y., Zheng, C. Y., et al., 2008. Geochemical Study of Crude Oils from the Xifeng Oilfield of the Ordos Basin, China. *Journal of Asian Earth Sciences*, 31(4/5/6): 341–356. <https://doi.org/10.1016/j.jseaes.2007.05.003>
- Fu, H. J., Yan, D. T., Yao, C. P., et al., 2022. Pore Structure and Multi-Scale Fractal Characteristics of Adsorbed Pores in Marine Shale: A Case Study of the Lower Silurian Longmaxi Shale in the Sichuan Basin, China. *Journal of Earth Science*, 33(5): 1278–1290. <https://doi.org/10.1007/s12583-021-1602-0>
- General Administration of Quality Supervision, Inspection and Quarantine of the People's Republic of China, 2003. Determination of Total Organic Carbon in Sedimentary Rock: GB/T 19145-2003. Standard Press of China, Beijing (in Chinese)
- Gu, Y. T., Li, X. X., Wan, Q., et al., 2021a. On the Different Characteristics of Organic Pores in Shale and Their Influencing Factors: Taking Typical Marine, Continental and Transitional Facies Reservoirs in China as Examples. *Acta Sedimentologica Sinica*, 39(4): 794–810 (in Chinese with English Abstract)
- Gu, Y. T., Li, X. X., Wan, Q., et al., 2021b. The Differential Evolution of

- Nanopores in Discrete OM and Organic-Clay Composites for Shale: Insights from Stress Manipulation. *Arabian Journal of Geosciences*, 14(7): 554. <https://doi.org/10.1007/s12517-021-06918-6>
- Guo, H. J., Jia, W., Peng, P. A., et al., 2014. The Composition and Its Impact on the Methane Sorption of Lacustrine Shales from the Upper Triassic Yanchang Formation, Ordos Basin, China. *Marine and Petroleum Geology*, 57: 509–520. <https://doi.org/10.1016/j.marpetgeo.2014.05.010>
- Hower, J., Eslinger, E. V., Hower, M. E., et al., 1976. Mechanism of Burial Metamorphism of Argillaceous Sediment: 1. Mineralogical and Chemical Evidence. *Geological Society of America Bulletin*, 87(5): 725–737. [https://doi.org/10.1130/0016-7606\(1976\)87725:mobmoa>2.0.co;2](https://doi.org/10.1130/0016-7606(1976)87725:mobmoa>2.0.co;2)
- Jia, W., Segal, E., Kornemandel, D., et al., 2002. Poly(aniline-DBSA)/Organophilic Clay Nanocomposites: Synthesis and Characterization. *Synthetic Metals*, 128(1): 115–120. [https://doi.org/10.1016/s0379-6779\(01\)00672-5](https://doi.org/10.1016/s0379-6779(01)00672-5)
- Jiang, Z., 2018. Pore Structure and Gas Bearing Property of Typical Marine and Continental Shale Reservoirs in China. Scientific Press, Beijing (in Chinese with English Abstract)
- Jiang, Q., Zhu, C., Qiu, N., et al., 2015. Paleo-Heat Flow and Thermal Evolution of the Lower Cambrian Qiongzhusi Shale in the Southern Sichuan Basin, SW China. *Natural Gas Geoscience*, 26(8): 1563–1570 (in Chinese with English Abstract)
- Kelemen, S. R., Fang, H. L., 2001. Maturity Trends in Raman Spectra from Kerogen and Coal. *Energy & Fuels*, 15(3): 653–658. <https://doi.org/10.1021/ef0002039>
- Kennedy, M. J., Droser, M., Mayer, L. M., et al., 2006. Late Precambrian Oxygenation: Inception of the Clay Mineral Factory. *Science*, 311(5766): 1446–1449. <https://doi.org/10.1126/science.1118929>
- Kennedy, M. J., Löhner, S. C., Fraser, S. A., et al., 2014. Direct Evidence for Organic Carbon Preservation as Clay-Organic Nanocomposites in a Devonian Black Shale: From Deposition to Diagenesis. *Earth and Planetary Science Letters*, 388: 59 – 70. <https://doi.org/10.1016/j.epsl.2013.11.044>
- Kennedy, M. J., Pevear, D. R., Hill, R. J., 2002. Mineral Surface Control of Organic Carbon in Black Shale. *Science*, 295: 657–660. <https://doi.org/10.1126/science.1066611>
- Kennedy, M. J., Wagner, T., 2011. Clay Mineral Continental Amplifier for Marine Carbon Sequestration in a Greenhouse Ocean. *Proceedings of the National Academy of Sciences of the United States of America*, 108(24): 9776–9781. <https://doi.org/10.1073/pnas.1018670108>
- Lagaly, G., 1989. Principles of Flow of Kaolin and Bentonite Dispersions. *Applied Clay Science*, 4(2): 105 – 123. [https://doi.org/10.1016/0169-1317\(89\)90003-3](https://doi.org/10.1016/0169-1317(89)90003-3)
- Lanson, B., Sakharov, B. A., Claret, F., et al., 2009. Diagenetic Smectite-to-Illite Transition in Clay-Rich Sediments: a Reappraisal of X-Ray Diffraction Results Using the Multi-Specimen Method. *American Journal of Science*, 309(6): 476–516. <https://doi.org/10.2475/06.2009.03>
- Li, S. Y., He, H. P., Tao, Q., et al., 2020. Kaolinization of 2 : 1 Type Clay Minerals with Different Swelling Properties. *American Mineralogist*, 105(5): 687–696. <https://doi.org/10.2138/am-2020-7339>
- Liu, A. Q., Tang, D. J., Shi, X. Y., et al., 2019. Growth Mechanisms and Environmental Implications of Carbonate Concretions from the ~1.4 Ga Xiamaling Formation, North China. *Journal of Palaeogeography*, 8(1): 1–16. <https://doi.org/10.1186/s42501-019-0036-4>
- Liu, D., Xiao, X., Tian, H., et al., 2012. Sample Maturation Calculated Using Raman Spectroscopic Parameters for Solid Organics: Methodology and Geological Applications. *Chinese Science Bulletin*, 58(11): 1285–1298 (in Chinese)
- Liu, S. G., Deng, B., Zhong, Y., et al., 2016. Unique Geological Features of Burial and Superimposition of the Lower Paleozoic Shale Gas across the Sichuan Basin and Its Periphery. *Earth Science Frontiers*, 23(1): 11–28 (in Chinese with English Abstract)
- Liu, Z. X., Xu, L. L., Wen, Y. R., et al., 2022. Accumulation Characteristics and Comprehensive Evaluation of Shale Gas in Cambrian Niutitang Formation, Hubei. *Earth Science*, 47(5): 1586 – 1603. <https://doi.org/10.3799/dqkx.2021.214> (in Chinese with English Abstract)
- Loucks, R. G., Reed, R. M., Ruppel, S. C., et al., 2009. Morphology, Genesis, and Distribution of Nanometer-Scale Pores in Siliceous Mudstones of the Mississippian Barnett Shale. *Journal of Sedimentary Research*, 79(12): 848–861
- Lu, L. F., Cai, J. G., Liu, W. H., et al., 2013. Occurrence and Thermostability of Absorbed Organic Matter on Clay Minerals in Mudstones and Muddy Sediments. *Oil & Gas Geology*, 34(1): 16–26 (in Chinese with English Abstract)
- Metwally, Y. M., Chesnokov, E. M., 2012. Clay Mineral Transformation as a Major Source for Authigenic Quartz in Thermo-Mature Gas Shale. *Applied Clay Science*, 55: 138 – 150. <https://doi.org/10.1016/j.clay.2011.11.007>
- Meunier, A., Velde, B., 1989. Solid Solutions in I/S Mixed-Layer Minerals and Illite. *American Mineralogist*, 74(9/10): 1106–1112
- Milliken, K. L., Rudnicki, M., Awwiller, D. N., et al., 2013. Organic Matter-Hosted Pore System, Marcellus Formation (Devonian), Pennsylvania. *AAPG Bulletin*, 97(2): 177–200
- National Energy Administration, 2010. Analysis Method for Clay Minerals and Ordinary Non-Clay Minerals in Sedimentary Rocks by the X-ray Diffraction: SY/T 5163-2010. Petroleum Industry Press, Beijing (in Chinese)
- O'Brien, N. R., 1971. Fabric of Kaolinite and Illite Floccules. *Clays and Clay Minerals*, 19(6): 353–359. <https://doi.org/10.1346/ccmn.1971.0190603>
- Rahman, H. M., Kennedy, M., Löhner, S., et al., 2018. The Influence of Shale Depositional Fabric on the Kinetics of Hydrocarbon Generation through Control of Mineral Surface Contact Area on Clay Catalysis. *Geochimica et Cosmochimica Acta*, 220: 429 – 448. <https://doi.org/10.1016/j.gca.2017.10.012>
- Schoenher, J., Litke, R., Urai, J. L., et al., 2007. Polyphase Thermal Evolution in the Infra-Cambrian Ara Group (South Oman Salt Basin) as Deduced by Maturity of Solid Reservoir Bitumen. *Organic Geochemistry*, 38(8): 1293 – 1318. <https://doi.org/10.1016/j.orggeochem.2007.03.010>
- Song, D. J., Tuo, J. C., Wang, Y. T., et al., 2019. Research Advances on Characteristics of Nanopore Structure of Organic-Rich Shales. *Acta Sedimentologica Sinica*, 37(6): 1309–1324 (in Chinese with English Abstract)
- Sposito, G., Skipper, N. T., Sutton, R., et al., 1999. Surface Geochemistry of the Clay Minerals. *Proceedings of the National Academy of Sciences of the United States of America*, 96(7): 3358 – 3364. <https://doi.org/10.1073/pnas.96.7.3358>
- Środoń, J., 2006. Chapter 12.2 Identification and Quantitative Analysis of Clay Minerals. Developments in Clay Science. In: Bergaya, F., Theng, B. K. G., Lagaly, G., eds., Developments in Clay Science. Elsevier, Amsterdam. 765–787. [https://doi.org/10.1016/s1572-4352\(05\)01028-7](https://doi.org/10.1016/s1572-4352(05)01028-7)
- Theng, B. K. G., Churchman, G. J., Newman, R. H., 1986. The Occurrence of Interlayer Clay-Organic Complexes in Two New Zealand Soils. *Soil Science*, 142(5): 262 – 266. <https://doi.org/10.1097/00010694-198611000-00003>
- Tosca, N. J., Johnston, D. T., Mushegian, A., et al., 2010. Clay Mineralogy,

- Organic Carbon Burial, and Redox Evolution in Proterozoic Oceans. *Geochimica et Cosmochimica Acta*, 74(5): 1579–1592. <https://doi.org/10.1016/j.gca.2009.12.001>
- Tuschel, D., 2013. Raman Spectroscopy of Oil Shale. *Spectroscopy*, 28(3): 20–28
- Wang, P. F., Jiang, Z., Chen, L., et al., 2016. Pore Structure Characterization for the Longmaxi and Niutitang Shales in the Upper Yangtze Platform, South China: Evidence from Focused Ion Beam-He Ion Microscopy, Nano-Computerized Tomography and Gas Adsorption Analysis. *Marine and Petroleum Geology*, 77: 1323 – 1337. <https://doi.org/10.1016/j.marpetgeo.2016.09.001>
- Wang, X. Z., Gao, S. L., Gao, C., 2014. Geological Features of Mesozoic Lacustrine Shale Gas in South of Ordos Basin, NW China. *Petroleum Exploration and Development*, 41(3): 326–337. [https://doi.org/10.1016/s1876-3804\(14\)60037-9](https://doi.org/10.1016/s1876-3804(14)60037-9)
- Wang, Y. F., Zhai, G. Y., Liu, G. H., et al., 2021. Geological Characteristics of Shale Gas in Different Strata of Marine Facies in South China. *Journal of Earth Science*, 32(4): 725 – 741. <https://doi.org/10.1007/s12583-020-1104-5>
- Wang, Z. M., Jiang, Y. Q., Fu, Y. H., et al., 2022. Characterization of Pore Structure and Heterogeneity of Shale Reservoir from Wufeng Formation-Sublayers Long-11 in Western Chongqing Based on Nuclear Magnetic Resonance. *Earth Science*, 47(2): 490–504. <https://doi.org/10.3799/dqkx.2021.076> (in Chinese with English Abstract)
- Xu, M., 2013. Studies on the Complexation and Stability of Clay Minerals and Organic Matter: [Dissertation]. Nanjing University, Nanjing (in Chinese with English Abstract)
- Yang, H., Niu, X. B., Xu, L. M., et al., 2016. Exploration Potential of Shale Oil in Chang7 Member, Upper Triassic Yanchang Formation, Ordos Basin, NW China. *Petroleum Exploration and Development*, 43(4): 560–569. [https://doi.org/10.1016/s1876-3804\(16\)30066-0](https://doi.org/10.1016/s1876-3804(16)30066-0)
- Yang, Y., Lei, T. Z., Xing, L. T., et al., 2015. Oil Generation Abilities of Chemically Bound Organic Matter in Different Types of Organic Clay Complexes. *Petroleum Geology & Experiment*, 37(4): 487 – 493 (in Chinese with English Abstract)
- Yariv, S., Cross, H., 2002. Clay-Organic Complexes and Interaction. Marcel Dekker, New York
- Yuan, P., 2018. Unique Structure and Surface-Interface Reactivity of Nanostructured Minerals. *Earth Science*, 43(5): 1384 – 1407 (in Chinese with English Abstract)
- Zhao, J. H., Jin, Z. J., Jin, Z. K., et al., 2016. Lithofacies Types and Sedimentary Environment of Shale in Wufeng-Longmaxi Formation, Sichuan Basin. *Acta Petrolei Sinica*, 37(5): 572–586 (in Chinese with English Abstract)
- Zhu, H. J., Ju, Y. W., Huang, C., et al., 2020. Microcosmic Gas Adsorption Mechanism on Clay-Organic Nanocomposites in a Marine Shale. *Energy*, 197: 117256. <https://doi.org/10.1016/j.energy.2020.117256>
- Zhu, X. J., Cai, J. G., Liu, W. X., et al., 2016. Occurrence of Stable and Mobile Organic Matter in the Clay-Sized Fraction of Shale: Significance for Petroleum Geology and Carbon Cycle. *International Journal of Coal Geology*, 160/161: 1 – 10. <https://doi.org/10.1016/j.coal.2016.03.011>
- Zhu, X. J., Cai, J. G., Wang, G. L., et al., 2018. Role of Organo-Clay Composites in Hydrocarbon Generation of Shale. *International Journal of Coal Geology*, 192: 83 – 90. <https://doi.org/10.1016/j.coal.2018.04.002>